

# Identifying the Causal Network of Sea Level Variability Domains in the Southeast Pacific

An application of satellite altimetry

**Eike Martin Schütt**

Christian-Albrechts University of Kiel, Institute of Geography

Master program "Umweltgeographie und – management", 4th semester

Final report on the internship project in the sea level group at the Royal Netherlands Institute for Sea Research (NIOZ). (Supervisors: Carolina Machado Lima de Camargo & Aimée Slangen)

## Abstract

Accurate projections of sea level rise are highly important for decision makers and the population in the low-lying coastal zone. However, due to the complex causes for the variability of sea level, reliable regional predictions remain a challenge. Understanding local and regional factors that contribute to this variability will improve the understanding and predictability of sea level. Sea level variations can be caused by many different factors, e.g. local and remote variability of atmospheric or oceanic circulations causing wind stress anomalies or changes in temperature or salinity.

In this project, more than 26 years of satellite data measurements of monthly mean sea level anomalies and the dimensionality reduction algorithm deltaMaps (Fountalis et al. 2018, Falasca et al. 2019) to derive regions with similar SLV dynamics, so called domains. The sea level signals of the different domains are then fed into the causal inference algorithm PCMCI (Runge et al. 2019) to identify the causal network between the domains. A subset of the causal network in the Southeast Pacific is then analysed using current velocity data from the CMEMS' GLORYS reprocessing and wind and sea level pressure data from ERA5 provided by ECMWF. The results highlight the importance of the El Niño-Southern Oscillation (ENSO) on both atmospheric and oceanic processes and suggest that SLV patterns in the Southeast Pacific are sensitive to the "flavour" of ENSO. However, this data driven approach can not accurately determine and quantify the physical processes at work and some questions remain unanswered. An approach that couples observational data and modelling may help to overcome this constraint.

# 1 Introduction

Global mean sea level rise is accelerating (Nicholls and Cazenave. 2010; Oppenheimer et al. 2019). It reached  $3.6 \text{ mm yr}^{-1}$  in the period 2008-2015 and is expected to increase further. Accurate projections of sea level rise are highly important for decision makers and the population along the coast to implement effective adaption strategies. However, due to the complex causes for variations in sea level, reliable regional predictions remain a challenge. Understanding local and regional factors that contribute to this variability will improve the understanding and predictability of sea level (Church et al. 2010; Han et al. 2019).

Many processes contribute to sea level variability (SLV). Among them are changes in the density in response to changing temperature and/or salinity (steric sea level change), forcing through wind stress and on a larger spatial and temporal scale local and remote changes in the atmospheric and oceanic circulations (Han et al. 2017; Meyssignac et al. 2017). SLV is thus primarily a response to climatic variability (Han et al. 2019).

A major source for global climate variability is the El Niño-Southern Oscillation (ENSO), a recurring climate pattern that causes periodic anomalies in sea surface temperatures, the air pressure of the overlying atmosphere and sea level height in the central and eastern tropical Pacific. The reader is referred to Wang et al. (2017) for a review of the potential causes, feedback cycles and characteristics of the different ENSO cycles. ENSO is known to influence global climate through atmospheric teleconnections (e.g. Yuan et al. 2018; Falasca et al. 2019; Fahad et al. 2021; Wiedermann et al. 2021). Likewise, disturbances of the sea level are transferred within the Pacific directly through oceanic teleconnections (e.g. Kelvin and Rossby waves) and atmospheric teleconnections and air-sea interactions (e.g. ENSO related alongshore winds causing upwelling) (Pizarro et al. 2002; Vega et al. 2003; Wang et al. 2016).

While the drivers of SLV in the northeast Pacific have been studied relatively intensively, only few studies address SLV in the Southeast Pacific and their teleconnections (a short review is included in Han et al. (2019)). In this context, this study aims to investigate how SL perturbations at the time scales of months to years are transferred through different regions in the Southeast Pacific by identifying the causal network between these regions. For this purpose, more than 26 years of global satellite SLA measurements have been analysed. First, the dimensionality reduction algorithm deltaMaps (Falasca et al. 2019) was used to derive regions with similar SLV dynamics, so called domains. The sea level signals of the different domains were then fed into the causal inference algorithm PCMCi (Runge et al. 2019b) to identify the global causal SLA network. A subset of this network in the Southeast Pacific was then analysed using current velocity, wind, and sea level pressure data.

The next desction describes the datasets of the satellite altimetry data and other environmental variables and both the deltaMaps and PCMCi algorithms. In Section 3 results are presented. The majority of this chapter is devoted to the analysis and discussion of the causal network. Then, limitations and possible ways to further enhance the understanding of SLV are described in section 4, before the results are summarised in section 5.

## 2 Data & Methods

### 2.1 SLA data preparation

Gridded global monthly mean sea level anomaly data has been obtained from Archiving, Validation and Interpretation of Satellite Oceanographic data (AVISO)

(<https://www.aviso.altimetry.fr/en/data/products/sea-surface-height-products/global/gridded-sea-level-anomalies-mean-and-climatology.html#c10358>) for the period January 1993 – February 2020. The dataset is corrected for the inversed barometer (IB) effect and comes in a  $\frac{1}{4} \times \frac{1}{4}^\circ$  resolution. To reduce the required processing time, the dataset was resampled to a  $2 \times 2^\circ$  resolution. Additionally, seasonality and linear trends have been removed from the data since the focus of this work is on variability over time scales of months to years.

The AVISO multimission sea level anomaly dataset is a compilation of data from 13 satellites (AVISO. 2016). Since most of the satellites are not in a polar orbit, the revisit time increases towards the high latitudes. Areas where the monthly mean is computed from only a relatively small number of measurements (higher than  $66^\circ\text{S}$  and  $66^\circ\text{N}$ ) were therefore excluded from the analysis.

In several regions, the  $2 \times 2^\circ$  resolution still contained mesoscale eddies that introduce substantial variability to the dataset that masks the underlying climate fluctuations. To increase the signal-to-noise ratio, the dataset has been spatially smoothed by applying a  $3 \times 3$  pixel Gaussian kernel (i.e.  $6 \times 6^\circ$ ). This separates large-scale atmospheric forcings and ocean dynamics from mesoscale variability (Forget and Ponte. 2015; Meyssignac et al. 2017).

## 2.2 deltaMaps

DeltaMaps analyses spatiotemporal systems and identifies regions (domains), that influence the system dynamics in an essential way (Falasca et al. 2019). This network analysis method consists of two main parts: The identification of the domains and the inference of the functional network between the domains.

### 2.2.1 Domain identification

Domains are spatially contiguous regions that show a similar dynamic effect over time, or, in other words, have a highly correlated temporal activity at zero lag time (Fountalis et al. 2018). Grid cells are highly correlated if their Pearson cross-correlation is higher than a threshold  $\delta$ . Falasca et al. (2019) proposed to determine  $\delta$  by assessing the cross-correlation between a large number of random pairs of grid cells (10000 in this study). A one-sided z-test with a significance level  $\alpha$  specified by the user (0.1 in our case) returns all significant cross-correlations.  $\delta$  is then defined as the average cross-correlation of all significant correlations.

The local homogeneity is defined as the average Pearson cross-correlation between a grid cell and its  $K$  nearest neighbours (based on the haversine distance) (Fountalis et al. 2018; Falasca et al. 2019). Grid cells with the local homogeneity being a local maximum and larger than  $\delta$  are seeds for a domain. Therefore, neighbourhood size ( $K$ ) is the smallest possible size of a domain. A series of domain merging and expansion operations follows. Adjacent or overlapping domains are merged if their average pairwise cross-correlation of all cells (homogeneity of the domain) is higher than  $\delta$ . Next, each domain expands to the adjacent grid cell that maximises its homogeneity, as long as the resulting homogeneity is higher than the threshold. Iterative checks if merging operations are possible and expansions are continued until no further grid cells can be added to a domain.

The optimal size of  $K$  has been determined by the heuristic proposed by Falasca et al. (2019). Domains were constructed for  $K$  values between 4 (smallest number where neighbours in all directions of a grid cell are considered) and 30 and the results were compared with the Normalized Mutual Information (NMI).  $K$  was chosen so that the NMI is large for this  $K$  and for neighbouring values of  $K$  in order to avoid that the result is sensitive to fluctuations around the chosen  $K$  value.

### 2.2.2 Network inference

After the domains are identified, deltaMaps infers a functional network between the different domains. The network is called “functional” to emphasize that it does not reflect causalities. Instead, it is based on functional activity and correlations (Fountalis et al. 2018).

Pearson cross-correlations between the domains are calculated for the domain signals, which are the cumulative sea-level anomaly of each domain (Fountalis et al. 2018). To account for potential time lags  $\tau$  between the signals of different domains, correlations are computed over a specified lag range (here  $\pm 12$  months). Additionally, the significance of each correlation is estimated (accounts for autocorrelation and multiple testing problem, significance  $q=0.05$ ). Two domains are connected, if at least one cross-correlation at a specific lag is significant. An edge (i.e. the connection between two domains in the network) will be associated with all significant lag values within  $\pm 1SD$  of the lag where the cross-correlation is maximum. The directionality of the edge is derived from this range of significant lag values (e.g., if it includes 0 the edge is undirected, if all values are positive the edge goes from domain A to domain B and vice versa). Finally, the edge weight is calculated based on the covariance of the two domains for the lag with the highest cross-correlation. The strength of a domain (the nodes of the network) is the absolute sum of all edges of that domain.

*Table 1: Applied deltaMaps parameters.*

parameter	value
sample size for $\delta$ estimation	10000
$\alpha$	0.01
K	4-30
$\tau_{\max}$	12
q	0.05

## 2.3 PCMCI

DeltaMaps infers a functional network that is based on the cross-correlation between the different domains (Fountalis et al. 2018). Similar correlation and univariate regression approaches are commonly used in Earth system science. However, they are not suited to gain insights into the causal structures of the underlying system (Runge et al. 2019a; Runge et al. 2019b). To overcome this constraint several causal inference frameworks have been developed.

The first practicable formalization of causality definition from time series has been provided by Granger (1969). The basic principle of Granger causality is to model a time series  $Y$  using all available information except  $Y$ 's history. If a second model, which uses all information except the history of  $Y$  and a second variable  $X$  predicts  $Y$  less accurately, then  $Y$  is causally dependent on  $X$ , because  $X$  adds information to the prediction model. Although this concept is more than 50 years old and many new concepts have been introduced since then, causal discovery methods have not been used widely in Earth system science. This is because most methods have a low prediction power in high dimensional and large-scale time series datasets, which means that true causal links may remain undetected (Runge et al. 2019b). Efforts have been made to overcome these constraints and new data-driven causal methods have been developed, providing promising approaches (see Runge et al. (2019a) for an overview).

The relatively new PCMCI algorithm has a higher detection power than established methods even in high dimensional data with strong autocorrelation (Runge et al. 2019b) and is therefore well suited to infer the network between different SLV domains. PCMCI is based on the graphical causal model framework. It consists of two main steps and begins with a fully connected causal network graph.

The first step of PCMCI is the condition selection or PC<sub>1</sub> stage, a modification of the PC algorithm. Here, all irrelevant edges between variables are removed by iterative independence testing. In the first iteration, edges between variables without unconditional dependency are removed. In the following rounds, connections between variables that are conditionally independent given the causal parents of the variable are removed as well (for a detailed description of PC<sub>1</sub> consult Runge et al. (2019b)). In contrast to other algorithms, PC<sub>1</sub> conditions on a relatively small number of relevant conditions, which include the causal parents and some false-positives. The second step of PCMCI, the momentary conditional independence (MCI) test, addresses the false-positives by conditioning on the parents of both variables in the potential causal link. This detects indirect and common cause links and accounts for autocorrelation (Runge et al. 2019b).

The iterative low-dimensional tests allow a high detection rate compared to e.g. Lasso, PC or Granger causality and the MCI reliably controls the false-positives (Runge et al. 2019b). With this, the algorithm is suitable for large datasets. It should, however, be stressed that PCMCI assumes causal sufficiency (i.e. all direct common driver are observed), which is likely violated in our study, since external (atmospheric) forcings that trigger sea level responses are not included in our dataset.

Ultimately, PCMCI infers a network between the variables that includes both contemporaneous and causal links. Contemporaneous relations are derived from effects that occur simultaneously or at a lag lower than the sampling frequency, so that the directionality of the edge cannot be determined, whereas the lag of causal edges is measurable, allowing to infer the directionality of the effect (Runge et al. 2019a).

In this study, PCMCI has been applied with linear partial correlation as conditional independence metric. The algorithm is available in the Python package Tigramite (version 4.2, Tigramite. 2020).

## 2.4 Environmental data

### 2.4.1 Flow data

To investigate the interplay between flow anomalies and SLA, north- and eastward flow anomalies were derived from current velocities in the GLORYS12V1 monthly physical reanalysis (1993-2018, 1/12° horizontal resolution, 50 vertical levels. Available at [https://resources.marine.copernicus.eu/?option=com\\_csw&view=details&product\\_id=GLOBAL\\_REANALYSIS\\_PHY\\_001\\_030](https://resources.marine.copernicus.eu/?option=com_csw&view=details&product_id=GLOBAL_REANALYSIS_PHY_001_030)). The dataset has been resampled to 2° resolution to match the resolution of the SLA dataset and reduce computing power. Next, seasonality was removed from the dataset. Current anomalies were then derived by subtracting the average current velocity from the current velocity at each time step, grid cell and depth level. These values were then converted to flow anomalies by integrating over all depth levels and calculating the flow across a 1 km wide transect.

### 2.4.2 Wind and Sea Level Pressure

U- and v- surface wind components and surface level pressure (SLP) were taken from the ERA5 monthly reanalysis provided by ECMWF (Hersbach et al. 2020). The data was again resampled to a 2° resolution, before removing seasonality and calculating anomalies.

### 2.4.3 El Niño timeseries

The Niño3.4 SST index was used as an indicator for the strength of ENSO. This index is the area averaged SST anomaly from 5°S-5°N and 170-120°W and thus corresponds to the average equatorial SST anomalies roughly between the dateline and the South American coast. Monthly Niño3.4 are available from NOAA (available at [https://psl.noaa.gov/gcos\\_wgsp/Timeseries/Nino34/](https://psl.noaa.gov/gcos_wgsp/Timeseries/Nino34/)).

### 3 Results & Discussion

#### 3.1 DeltaMaps

Figure 1 shows the NMI plot for different combinations of the neighbourhood factor  $K$ . Some values of  $K$  appear to be a local maximum of NMI ( $K=7, 11, 16, 20$ ). However, the detected domains for large values of  $K$  cover only a small portion of the global ocean. Considering both the NMI and the area covered by domains,  $K = 7$  and  $K = 11$  have the best results, while the NMI around  $K = 11$  is more constant and was therefore selected for the rest of the analysis.

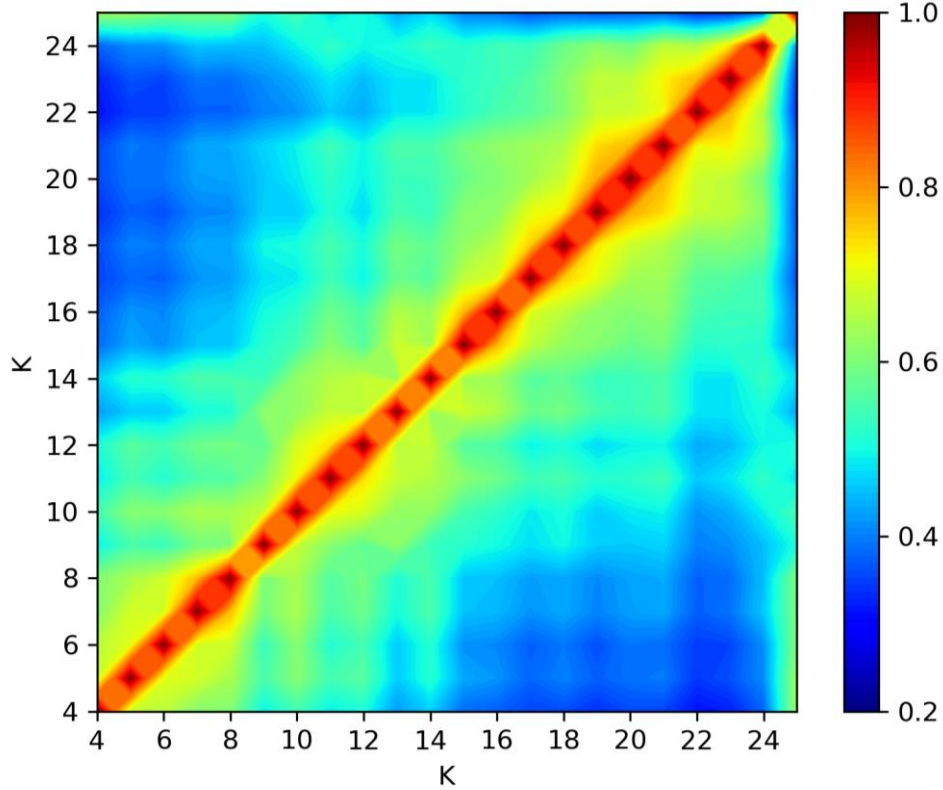


Figure 1: Normalized mutual information for different combinations of  $K$ .

With this parameter setting 101 SLV Domains were identified (Figure 2) and the network inferred by deltaMaps is shown in (Figure 3). Some of the edges in the network can be explained by well-known climate modes and sea level feedbacks.

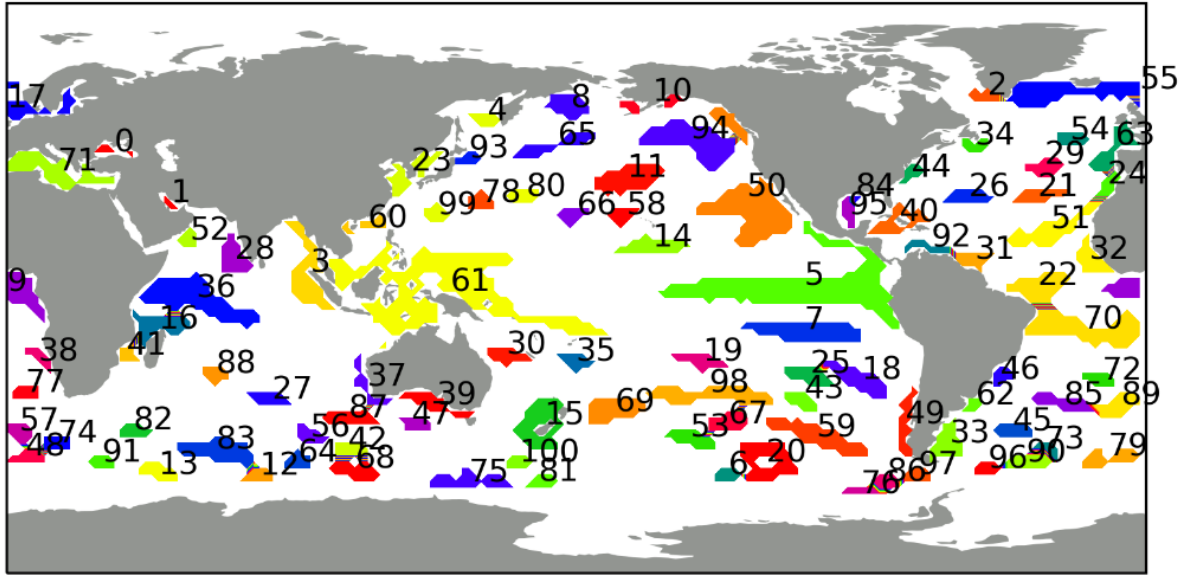


Figure 2: Detected domains for  $K = 11$ . Each domain is randomly coloured and labeled with the corresponding domain number.

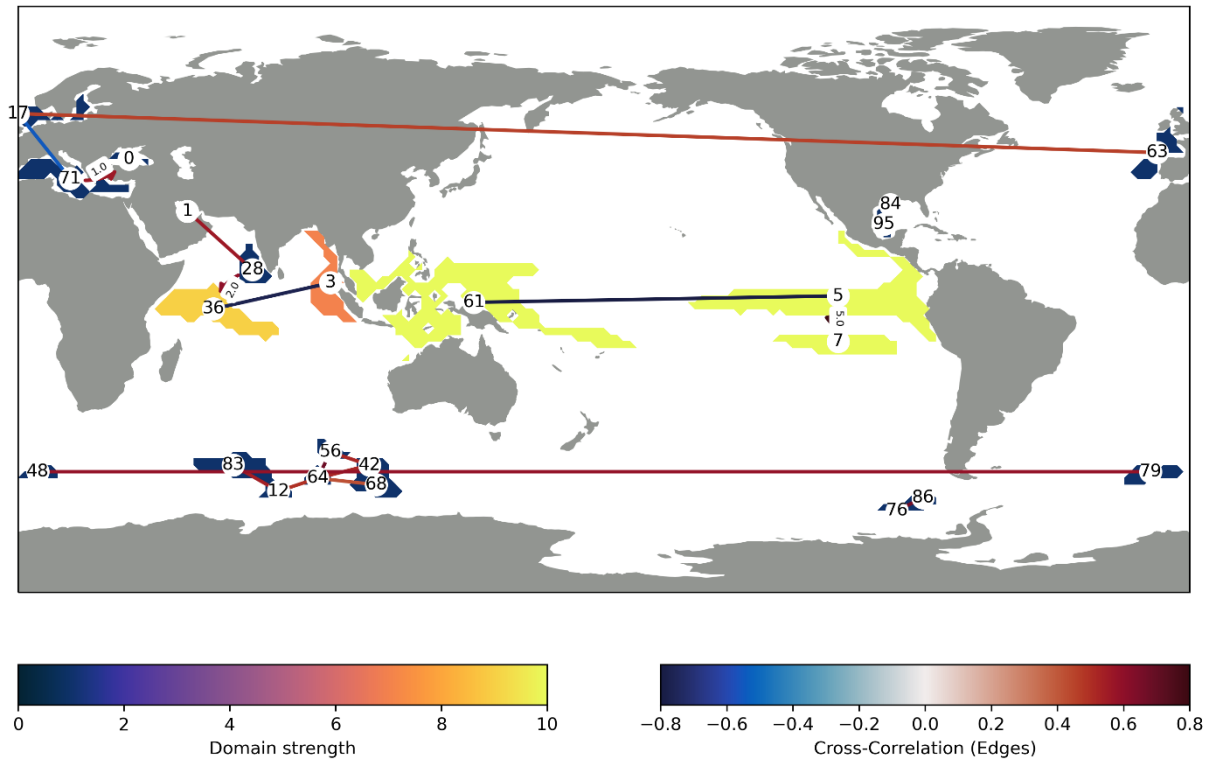


Figure 3: Network inferred by deltaMaps for  $k=11$ . Only domains with an edge are shown and coloured according to the Domain strength. The colour of the edges corresponds to the highest absolute cross-correlation of both domains. Domain IDs are indicated in round labels, while labels on the edges denote non-zero significant lag times (in months).

In the Pacific, the most prominent feature is the strong negative cross-correlation between domain signals of regions 5 (Eastern Tropical Pacific, ETP) and domain 61 (Western Tropical Pacific, WTP). The Pacific east-west sea level dipole variability is highly correlated with the El Niño-Southern Oscillation (ENSO) (Moon et al. 2015). SLAs in this region are mainly caused by surface wind anomalies (Ren et al. 2020). During the neutral ENSO phase, easterly trade winds cause water to accumulate in the WTP, which is enhanced during La Niña phases with its associated stronger than average easterly winds. In



the El Niño phase, surface winds are weakened or even reversed, causing sinking sea levels in the WTP and higher sea levels in the ETP.

In the Indian Ocean, the negative correlation between domains 3 (eastern tropical Indian Ocean) and 36 (western tropical Indian Ocean) mainly reflect influences of the Indian Ocean Dipole (IOD), an interannual coupled ocean-atmosphere climate mode with seasonal patterns and large interannual variability (Han et al. 2017). Similar to ENSO in the Pacific, IOD is also associated with an east-west dipole of Sea Surface Temperatures anomalies and surface wind anomalies (Palanisamy et al. 2014). In response to surface wind anomalies, sea level in the tropical Indian Ocean changes. Thermostatic sea level also contributes to the spatial patterns (Han et al. 2017).

Even though deltaMaps is able to detect some well-known connections of sea level variability, it has failed to reproduce other known linkages (e.g., ENSOs influence on coastal sea level along the west coast of the American continent (Vega et al. 2003; Hamlington et al. 2015; Han et al. 2019)). It should also be noted that most edges Figure 3 have no lag time.

The sparse deltaMaps network may be a result of the high dimensionality of the data (101 domains) and the high  $\tau_{\max}$  (12 months). deltaMaps addresses the multiple testing problem by controlling the rate of false positives with the False Discovery Rate (FDR) method (Fountalis et al. 2018). Apparently, only a small number of edges pass the FDR test. Therefore, the PCMCI algorithm has been applied, a causal network inference method with a high detection power even in high dimensional data (Runge et al. 2019b).

### 3.2 PCMCI

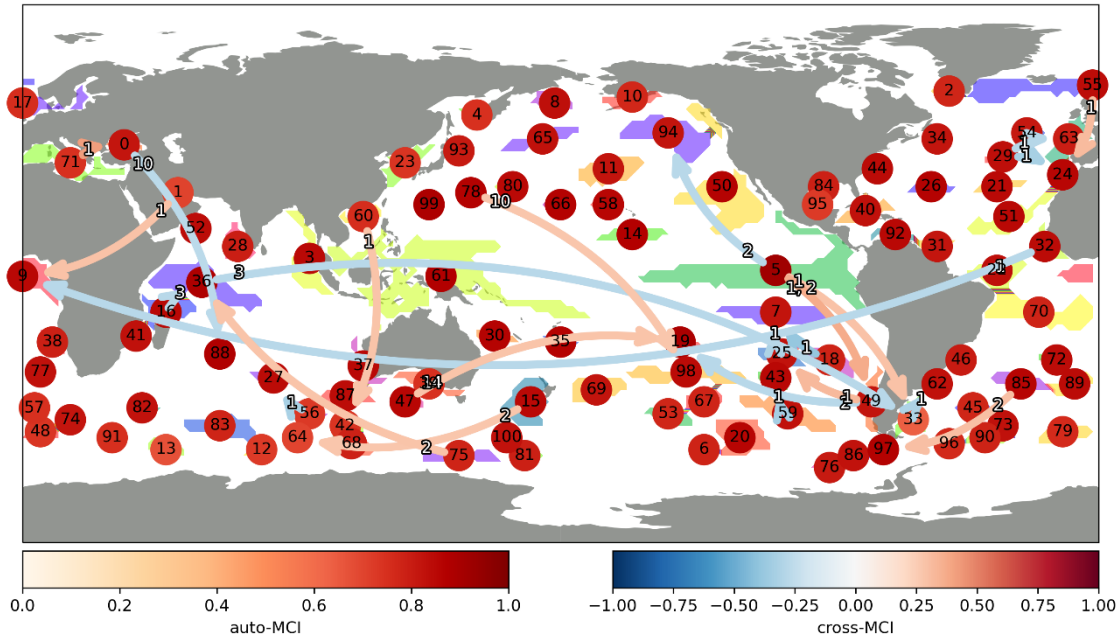


Figure 4: Causal network derived by the PCMCI between the different sea level variability domains. (PCMCI parameters:  $\tau_{\min}=1$ ,  $\tau_{\max}=15$ ,  $\alpha=0.01$ ). The node colour reflects the auto-momentary causal independence (MCI) while the edge colour shows the cross MCI. White numbers on the edges show the time lag in months. Note that this map only shows causal links (i.e. links with a time lag) and no contemporaneous links. Nodes are placed roughly in the middle of each domain. The domain extend is marked by radonmly cooloured areas in the background.

PCMCI identifies considerably more edges then deltaMap. It is not possible to show the global network with all contemporaneous and causal (i.e. lagged) edges in a meaningful plot. For this reason, Figure 4 shows only the causal links of the network. It becomes clear that the PCMCI result differs significantly from the deltaMaps functional network (Figure 3) in both density and structure.



Figure 5 shows both contemporaneous and causal links for the eastern tropical Pacific (ETP) sea level domain (domain 5). Similar to the deltaMaps network it reveals a negative connection between ETP and WTP (domain 61), which resembles the ENSO sea level dipole (Moon et al. 2015). It also produces consistent results by correctly identifying the teleconnections between ENSO and IOD (Domains 3 and 36; Yuan et al. 2018; Zhang et al. 2019).

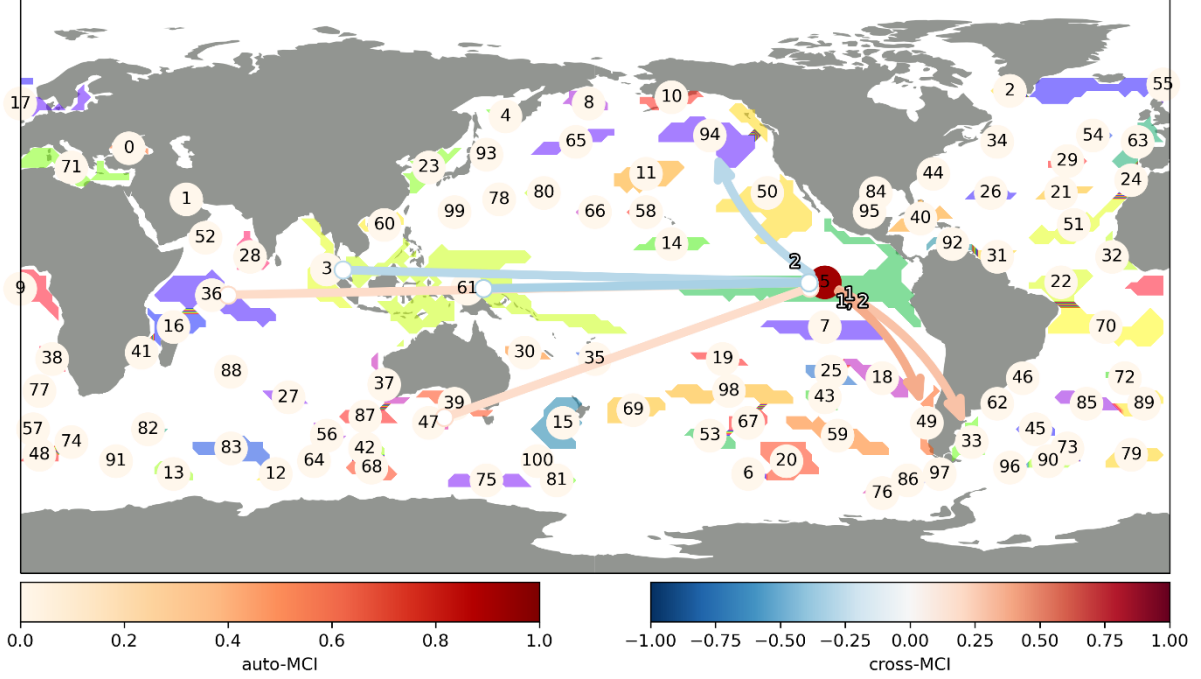


Figure 5: Contemporaneous and causal links to and from the ENSO domain. (PCMCI parameters:  $\tau_{min}=0$ ,  $\tau_{max}=15$ ,  $\alpha=0.01$ ).

### 3.3 Semi-circular causal SLV network in the Southeast Pacific Ocean

The Southeast Pacific Ocean shows an almost circular network (Fig. 5). From the ENSO domain (domain 5), the SLA signal propagates south towards Domain 49, the Domain off the Chilean coast, with a lag of 1 to 2 months. From there, a causal link to waters around the Easter Island (Domain 25) exists with a lag of 1 month. Domain 25 in turn negatively influences SL in Domain 7 at a lag of 1 month. Figure 6 shows the timeseries of the mean SLA signals in each of the Domains. In the following, drivers for each domain and their teleconnections will be identified and discussed.

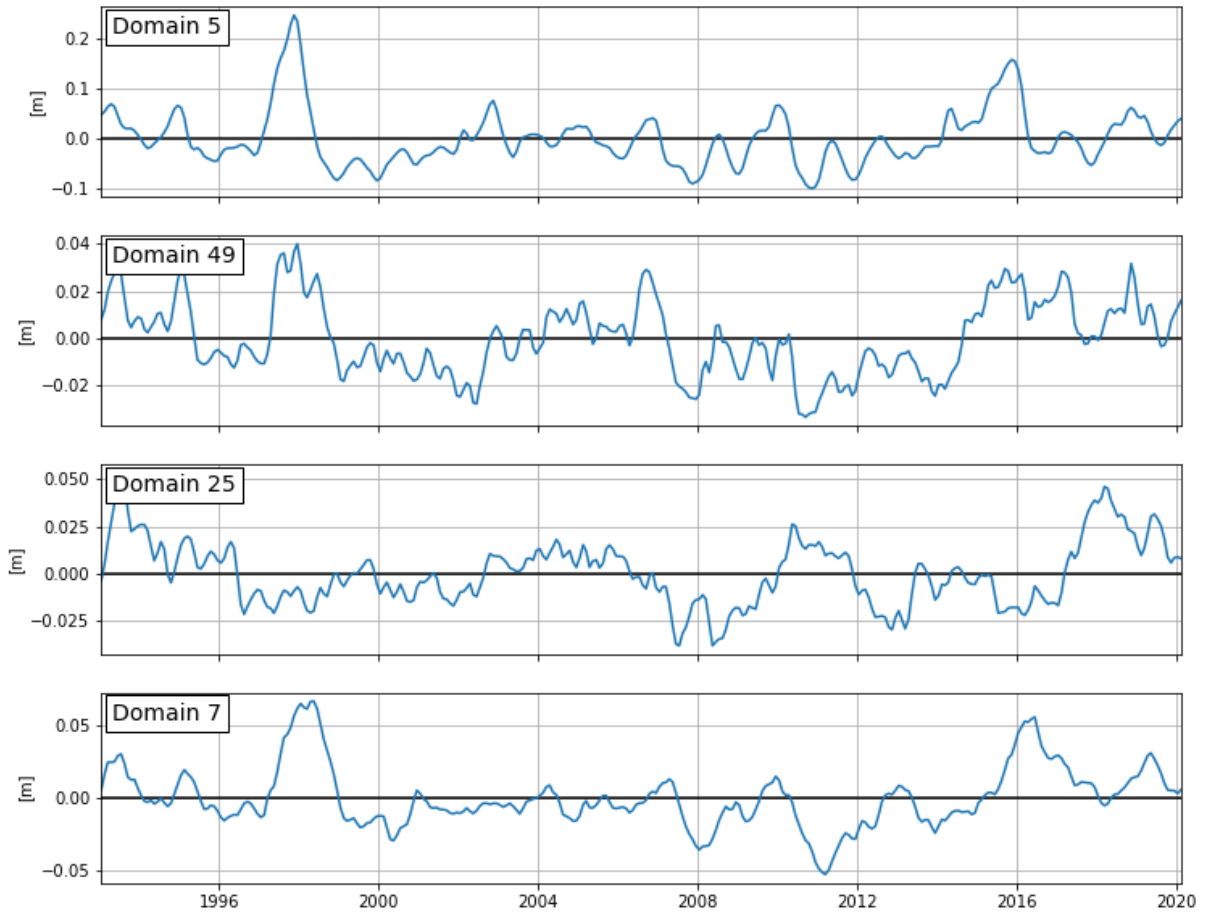


Figure 6: Mean SLA in different domains in the Southeast Pacific. Note the different scales on the y-axis. The black line indicates the mean sea level.

### 3.3.1 Edge between Domains 5 and 49

SLA in domain 5 (ETP) clearly reflects the patterns of the Niño3.4 index (see Figure 7). ENSO is known to be linked to the sea level in the tropical Pacific mainly through wind stress anomalies, but also through thermocline displacements and upper ocean geostrophic current anomalies (e.g. Hamlington et al. 2015; Han et al. 2017; Ren et al. 2020). Simply put, in the positive ENSO phase (El Niño phase) easterly trade winds weaken or reverse, which leads to a positive SLA in the eastern tropical Pacific, which, in turn, limits, together with the wind anomalies, the upwelling at the west coast of South America, which leads to higher SSTs. In contrast, the La Niña phase is associated with strengthened easterly trade winds and a sea level falls in the eastern tropical Pacific, thus causing enhanced upwelling at the Pacific's eastern boundary by this lower SSTs. A strong correlation between the Niño3.4 SST index and the SLA signal in this domain is therefore not surprising.

SLA in the eastern tropical Pacific is thought to influence the alongshore flow along the South American continent (Pizarro et al. 2002). This may explain the causal link from the ETP domain (domain 5) to the coastal domain off Chile (domain 49) at a lag of 1 and 2 months (Figure 5).

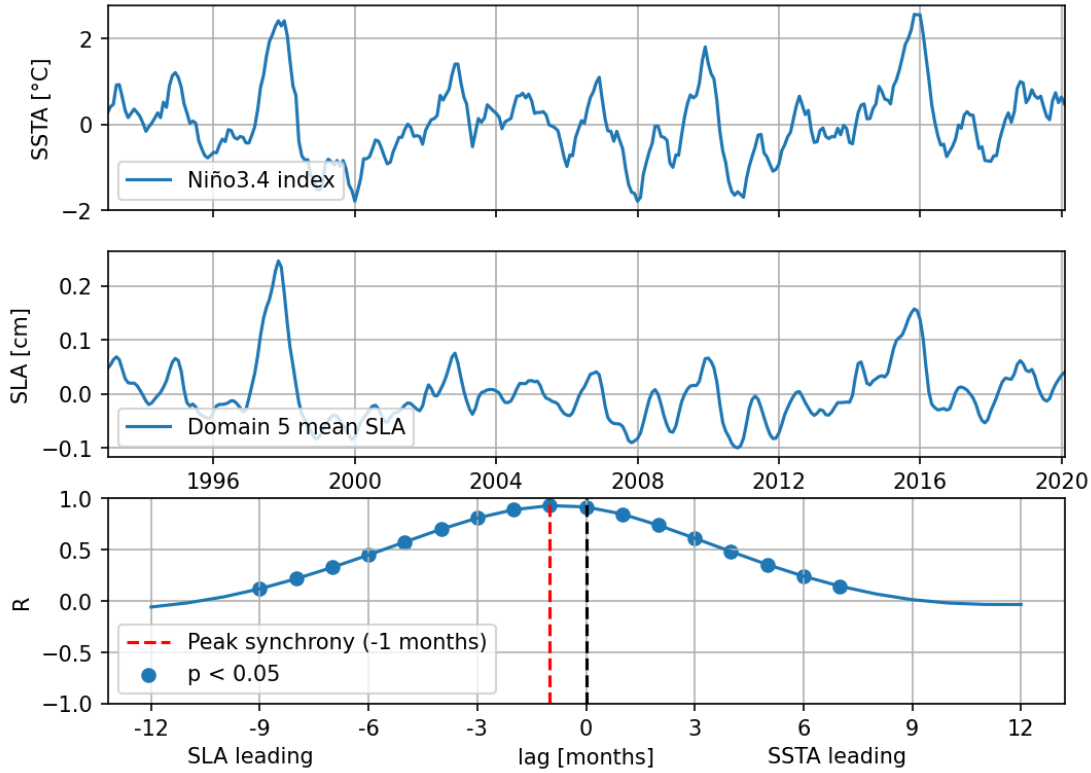


Figure 7: Time series of sea surface temperature anomalies (SSTA) in the Niño3.4 region (top), mean SLA in domain 5 (middle) and the lagged correlation (bottom). The blue points indicate significant correlations ( $p < 0.05$ ) and the red dashed line indicates the lag with the highest absolute correlation.

This effect of Domain 5 SLAs on the alongshore current can also be seen in flow anomaly data off Peru. Figure 8 shows that SLA in the ETP domain has a significant negative correlation to northward flow and a significant positive correlation to eastward flow at a peak synchrony of 3 and 4 months, respectively. This means that a high sea level in the ETP will usually be followed by a south-easterly (i.e., poleward) alongshore flow, likely caused by diffusion, which has also been observed by Li and Clarke (2007). However, the peak synchrony (3-4 months) is too large to explain the link between the ETP domain and Domain 49 (1-2 months) and the influence of ETPs SLA on alongshore flow fades further south (Figure 9).

The short lag time of the causal edge between domains 5 and 49 suggest that domain 49 is connected to domain 5 through relatively fast ( $2.5\text{--}3\text{ m s}^{-1}$ ) coastal waves, which are known to occur along this coast (Pizarro et al. 2001; Peng et al. 2019). These waves originate from the tropical Pacific, where trade wind anomalies (e.g. the weakening of winds in the central Pacific or westerly wind bursts (WBB) in the early stages of an El Niño phase) force equatorial Kelvin waves that propagate eastwards along the equator (Wang et al. 2016; Peng et al. 2019). When they impinge on the eastern ocean boundary, they get coastally trapped and propagate the disturbance poleward (Han et al. 2019). A coastally trapped wave takes  $\sim 20$  days from the equator to  $33^\circ\text{S}$ , the northern end of domain 49 (Pizarro et al. 2002; Hughes et al. 2019). Taking into account that disturbances first travel a certain distance along the equator as equatorial Kelvin waves in domain 5 (depending on where they were generated,  $\sim 32$  days from the western tip of domain 5 at  $150^\circ\text{W}$  until reaching the eastern boundary at a speed of  $2.8\text{ m s}^{-1}$ , Wang et al. 2016), the travel time matches the lag time of the causal link between domains 5 and 49 remarkably well.

Modelling results by Pizarro et al. (2001) suggest that SLV along the South American coast can primarily be explained by this remote equatorial forcing. Anomalies in alongshore wind stress are less important but still relevant and will be discussed in the next section.

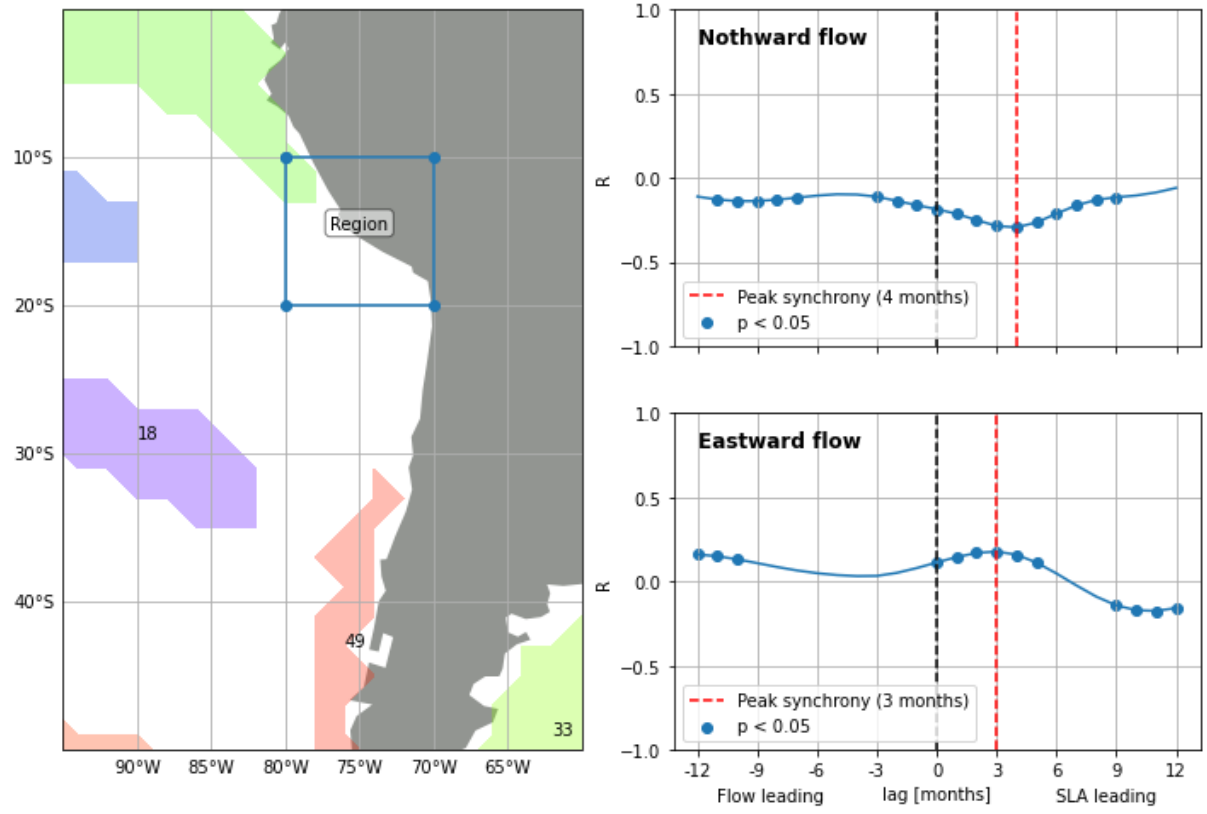


Figure 8: Correlation between mean northward and eastward flow in the region encircled in blue and SLA in the ETP domain (Domain 5) at different lag times. Meaning of points and lines is the same as in Figure 7.

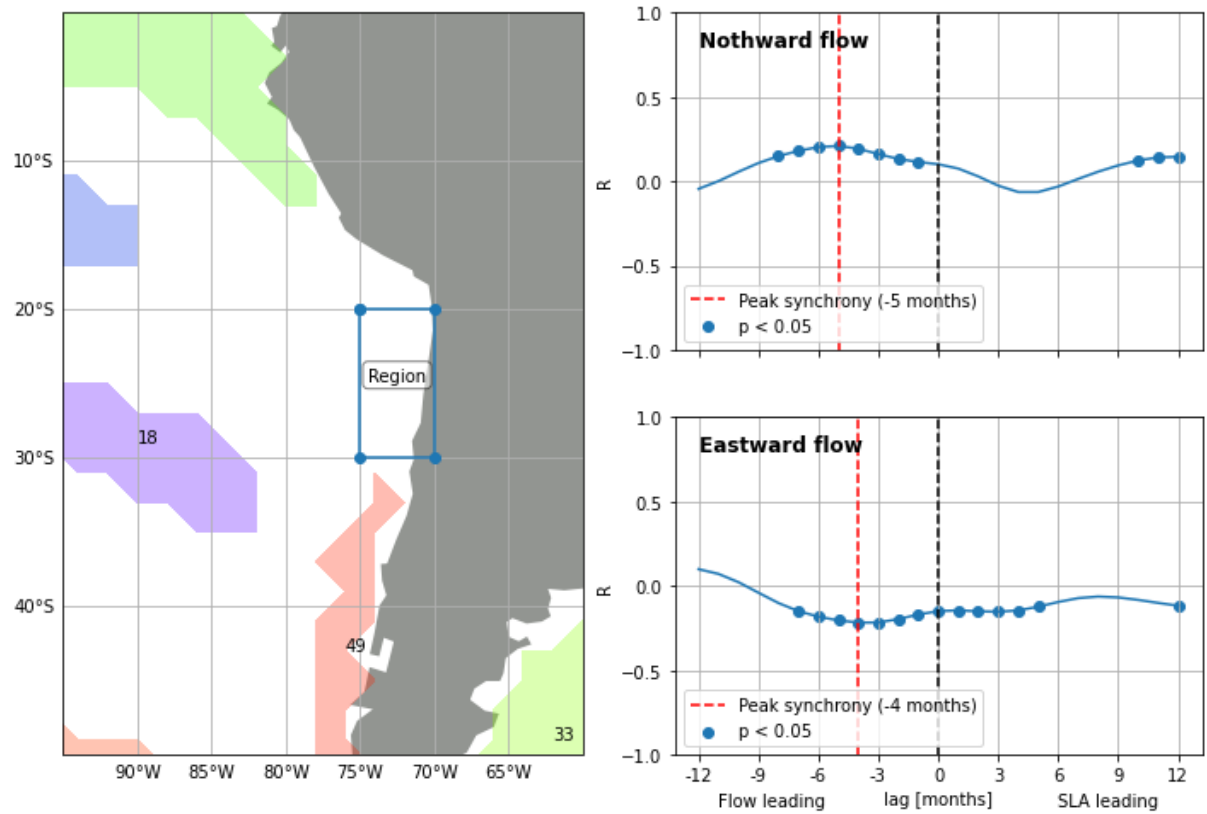


Figure 9: Same as Figure 7, but for a more southerly region.

### 3.3.2 Edge between Domains 49 and 25

Comparing the time series of domains 49 and 25 by eye, shows notable differences and no clear relationship (Figure 6). During some periods, SLAs in Domain 49 and 25 appear to be anti-correlated (usually with Domain 49 showing positive/negative and Domain 25 negative/positive SLAs during El Niño/La Niña), while during other periods SLAs in both domains are remarkably in-phase. PCMCi inferred both a positive contemporaneous link (cross-MCI 0.214) and a positive causal link from domain 49 to domain 25 at a lag time of one month (cross-MCI 0.282, Figure 4).

Coastal trapped waves excite westward propagating Extratropical Rossby Waves (ETRW) under certain circumstances so that an equatorial signal propagates both poleward along the shore and offshore (Pizarro et al. 2002). However, compared to coastal trapped waves, ETRW have a low phase speed that increases with latitude (Ramos et al. 2008). Observations from Vega et al. (2003) suggests that ETWRs take  $\sim 7$  months from the coast to the centre of Domain 25 (observed phase speed at  $27^\circ\text{S}$  of  $0.05 \text{ m s}^{-1}$ ) and can thus be ruled out as a cause for the links between Domains 49 and 25 at zero and one month lag.

It can be seen in Figure 10 that the link between Domains 49 and 25 is also not caused by characteristic flow patterns between the two domains. Only the eastward component, which is directed away from domain 25, is significantly but weakly ( $R < 0.25$ ) correlated to domain 25 SLAs at -1- and 0-months lag.

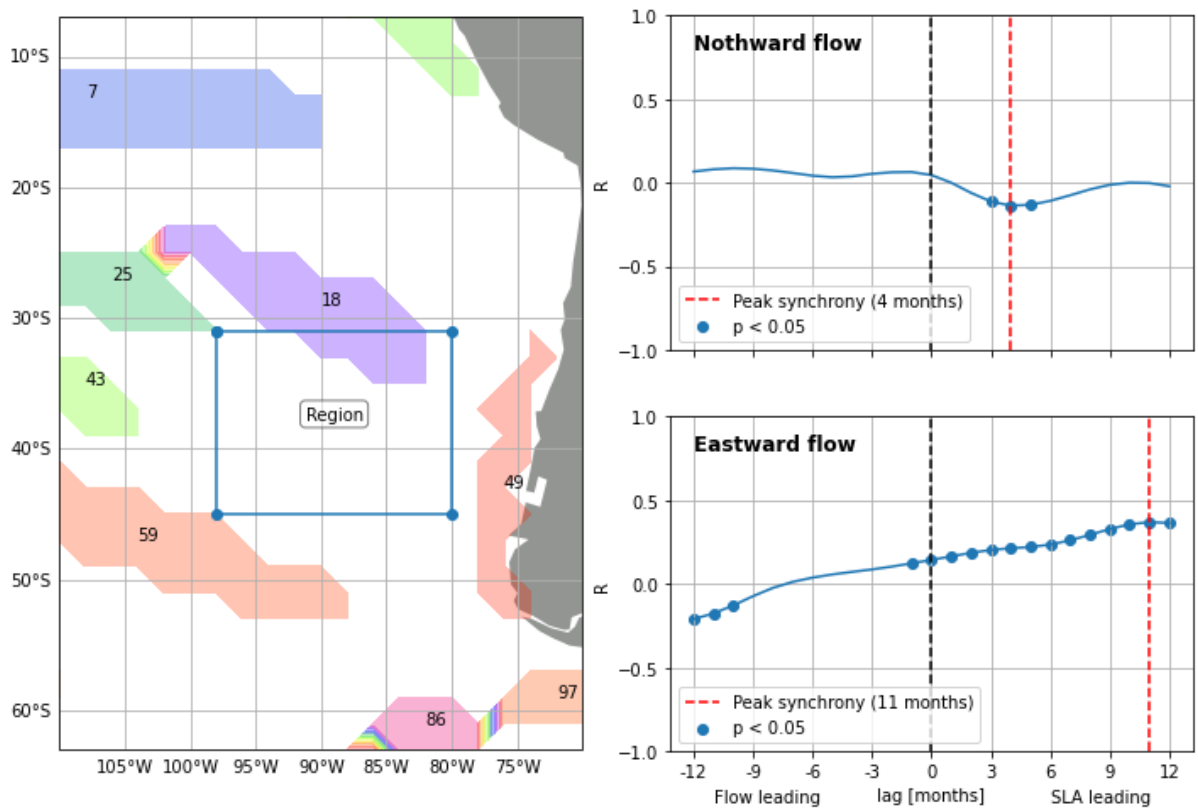


Figure 10: Correlation between mean northward and eastward flow in the area encircled in blue and the SLA in domain 25 for different time lags. Symbol meaning is the same as in Figure 7.

Due to the low lag time of 0 and 1 month between both domains, it can be hypothesized that both Domains are connected through an atmospheric process, which act on faster time scales than oceanic teleconnections. Indeed, the SL signal in domain 25 is significantly correlated to surface wind stress anomalies and their direction around and inside the domain (Figure 11). An anticlockwise rotation of wind stress anomalies around the domain will cause a positive SLA, likely as a result of Ekman transport towards the centre of this rotation. Such wind patterns are caused by the Southeast Pacific Subtropical

Anticyclone (SPSA), the dominant weather system in the Southeast Pacific. Its semi-permanent centre is typically a few degrees southeast of domain 25 (marked with “H” in Figure 11, varies between 28-36 °S and 85-108°W on decadal timescales; Ancapichun and Garcés-Vargas. 2015). SLA in Domain 25 is also significantly correlated to mean pressure anomalies in Domain 18 (which represents the mean position of the SPSA relatively well; Figure 12) and therefore appears to be sensitive to the position, winds stress and Ekman flow associated with SPSA.

The strength and position of SPSA shows regular seasonal patterns. Interannual to -decadal is primarily modulated by ENSO and to smaller extends by the Southern Annular Mode (SAM) and Pacific Decadal Oscillation (PDO) (Fuenzalida et al. 2008; Ancapichun and Garcés-Vargas. 2015). Ancapichun and Garcés-Vargas (2015) found that ENSO negatively influences SPSA strength. This means that during positive/negative ENSO events (El Niño/La Niña), the SLP of the SPSA is lower/higher, which causes weaker/stronger than average anticlockwise wind stress around the centre of SPSA and thus less/more Ekman transport towards the high-pressure centre. This atmospheric teleconnection and air-sea interaction explains why SL in Domain 25 often appears to be anti-correlated to ENSO strength.

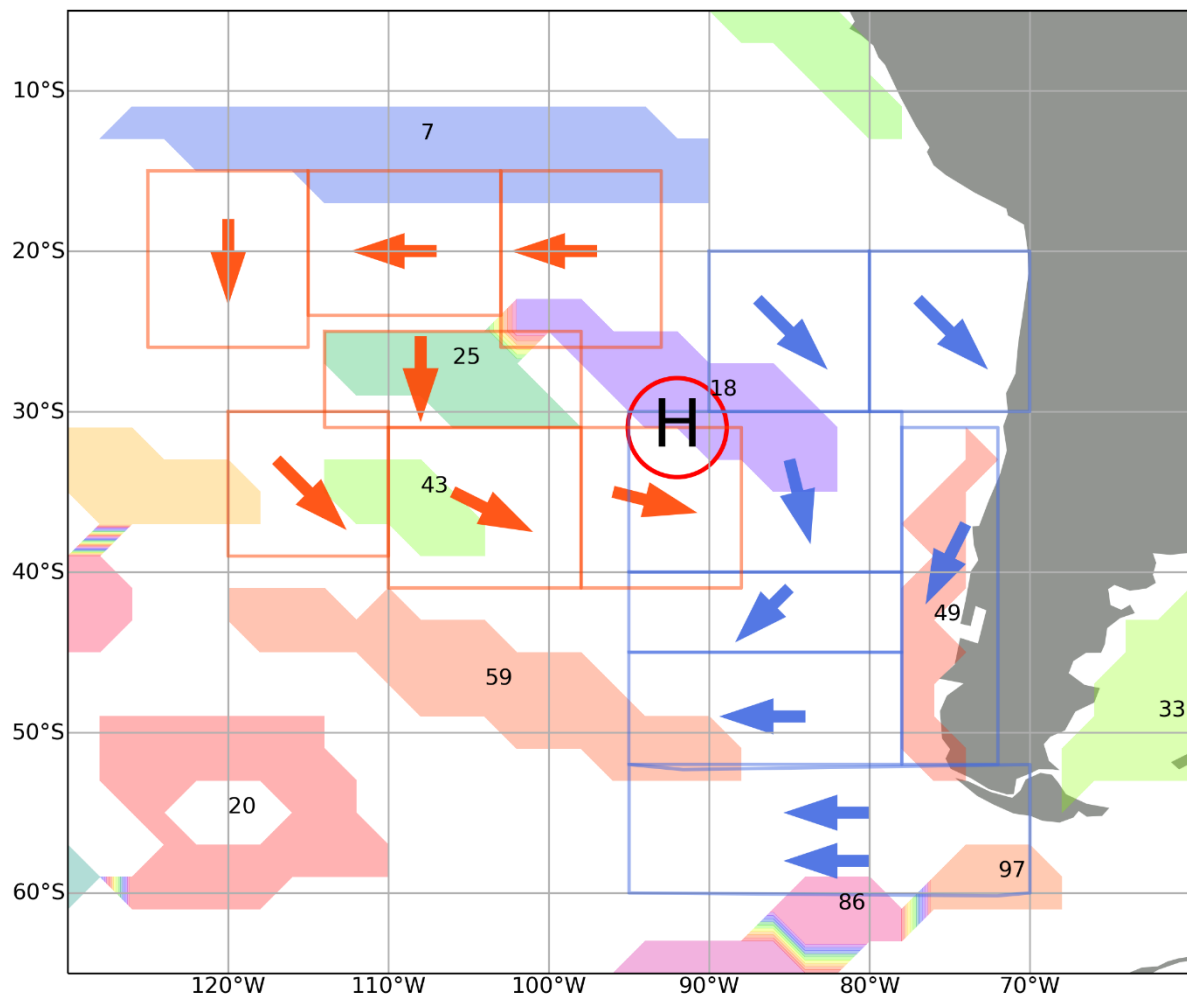


Figure 11: Surface wind stress directions (arrows) in different regions around Domains 49 (blue) and 25 (orange) with a significant correlation to SLA in the respective domains at low lag (1 and/or 0 months). The red encircled “H” marks the position of the maximum average SLP (1993-2020) in the ERA5 dataset and can thus be interpreted as the mean centre of the Southeast Pacific Subtropical Anticyclone (SPSA).

The intensity of SPSA also influences currents along the South American coast (Fuenzalida et al. 2008). Indeed, SPSA strength and SLA in Domain 49 show a significant negative lagged correlation, where SLP leads by 2 months ( $R > 0.5$ , figures in [Supplementary](#)). If SPSA is stronger than usual, northerly

alongshore winds increase and thus also westward Ekman transport, which would cause a drop of the coastal sea level (and upwelling) and vice versa. Given that SPSA strength is modulated by ENSO strength, this effect amplifies the equatorial forcing through the oceanic teleconnection.

SLV in both domains 49 and 25 appear to be modulated by surface winds controlled by the SPSA. However, as SPSA intensity is negatively correlated to SLA in Domain 49 but positively to SL in Domain 25, it does not explain the significant positive cross-MCIs between both Domains. Indeed, SLA in Domain 49 appears to oppose SLA in Domain 25 especially during positive (e.g. 1997/98 or 2015/16) and negative ENSO events (e.g. 2011/12 or 2017/18, Figure 6).

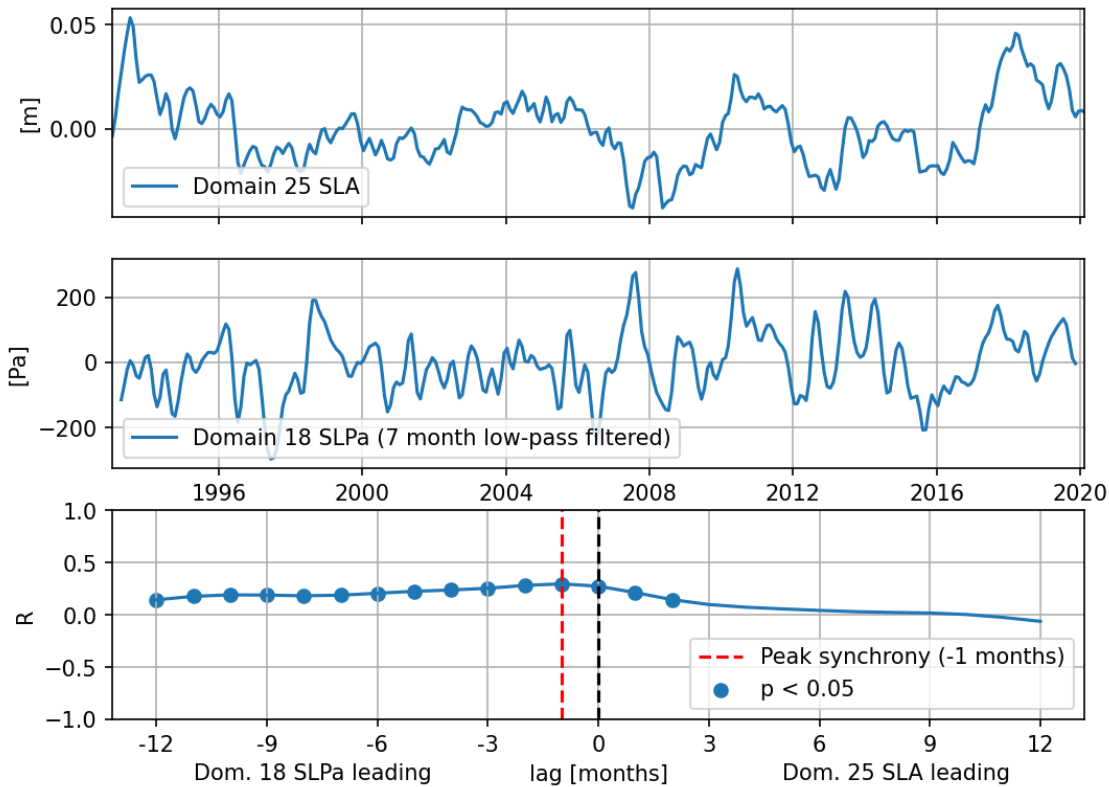


Figure 12: Timeseries of mean SLA in Domain 25 (top), mean atmospheric surface pressure anomaly in Domain 18 (middle, indicator for SPSA strength) and lagged correlation for different lags between the two time series (bottom). Symbol meaning is the same as in Figure 7.

This “out-of-phase” relation is, however, not continuous. Several periods with lengths in the order of a few months to years exists where SLAs in both Domains are surprisingly similar (see the light red areas in Figure 13a for examples). Synoptic SLP and wind stress anomalies of these periods reveal that a coupled increase of SL in both Domains often coincides with relatively strong cyclonic pressure anomalies at the border from the Southeast Pacific to the Southern Ocean (south of 30-40°S and west of 80°W) and clockwise wind stress anomalies around the SLP anomaly. In all four examples in Figure 13, SLP is around normal north of 30°S. The clockwise wind stress anomalies enhance the westerly winds south of domain 25. West of Domain 49, the wind stress anomalies are turning to a northerly direction and to easterly wind stress anomalies south of Domain 49. This pattern partly resembles the one in Figure 11 and causes Ekman transport towards both Domains and thus causes SL to rise almost simultaneously.

Both domains SLA signals show a significant negative lagged correlation to the mean SLP in Domain 59, which roughly coincides with the area where the SLP anomaly is situated in the four examples in Figure 13 (figure in [Supplementary](#)). This adds further confidence that negative SLP anomalies and associated wind stress and Ekman transport anomalies south of 30°S are responsible for a temporary coupling of



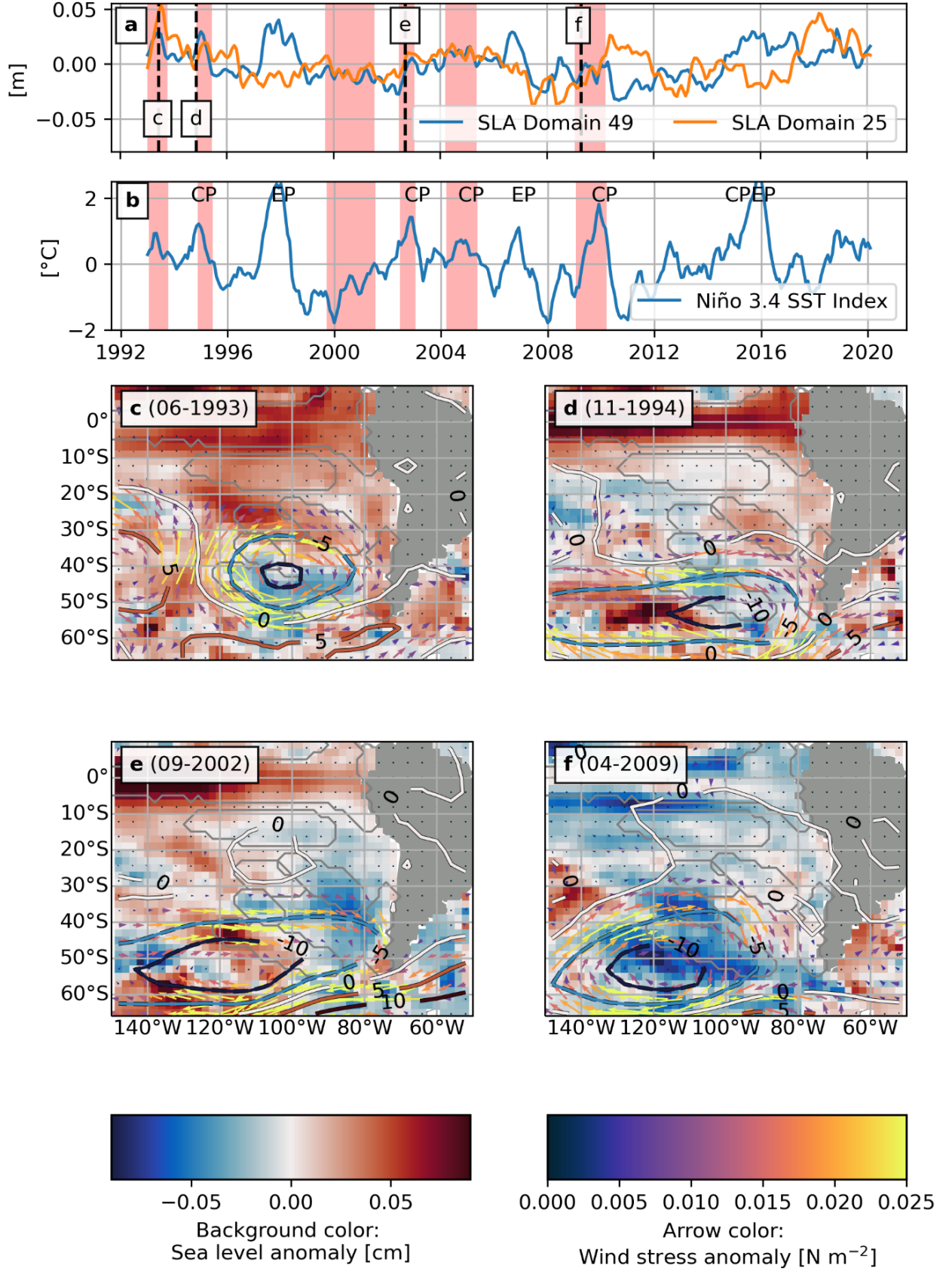


Figure 13: Timeseries of SLA in Domains 49 and 25 (a). The red areas highlight periods where both SLA signals are relatively similar. The dashed black lines and letters mark the times of the anomaly maps below. B shows the Niño3.4 SST index. Labels CP and EP denote Central Pacific and Eastern Pacific flavours of El Niño events, respectively (according to Wiedermann et al. 2021). The maps (c-f) show anomalies of SL (background color), SLP (blue/red isolines with labels in hPa) and wind stress (arrows). Gray contours denote the different Domains.

SLA signals along the coast of Chile (Domain 49) and in the central Southeast Pacific (Domain 25). This process is likely responsible for the positive links at zero- and one-month lag between the two domains. No other process, that connects both domains in a positive way, was found.

The temporal shift in the relation of Domain signals 49 and 25 appears to be triggered by the “flavour” of ENSO (Figure 13). During East Pacific (EP) El Niño, SST anomalies are highest in the eastern tropical Pacific, whereas during Central Pacific/Modoki El Niño SST is highest in the central tropical Pacific around the dateline (Kao and Yu. 2009; You and Furtado. 2017). Both types of ENSO events affect the earth systems differently, which has gained much attention over the last decade (e.g. Dewitte et al. 2012; Wilson et al. 2014; Conejero et al. 2020; Wiedermann et al. 2021). Wilson et al. (2014) found that the strength of the blocking in the SEP (stronger/weaker during EP/CP events) and SLP anomalies in the Drake passage are associated with the flavour of ENSO. Recently Fahad et al. (2021) suggested that these regions are connected through the South Pacific Convergence Zone (SPCZ) and atmospheric Rossby wave trains, but many questions on this atmospheric teleconnection remain unanswered. Nevertheless, it appears likely, that EP El Niño events trigger distinct SLP and wind stress anomaly patterns in the southern part of the Southeast Pacific and the Drake passage, which also shifts the SLA relation between the South American coast and the central Southeast Pacific.

### 3.3.3 Edge between Domains 25 and 7

The relationship of Domains 25 and 7 features two significant links: A positive contemporaneous link (cross-MCI 0.267) and a negative link at one month lag time, directed from Domain 25 to Domain 7 (cross-MCI -0.306, Figure 14). However, both Domain signals are not significantly lag-correlated at small lags ( $< 3$  months, [figure in Supplementary](#)). First, the main drivers for the SL dynamics in Domain 7 will be identified, before the links between Domains 25 and 7 will be discussed.

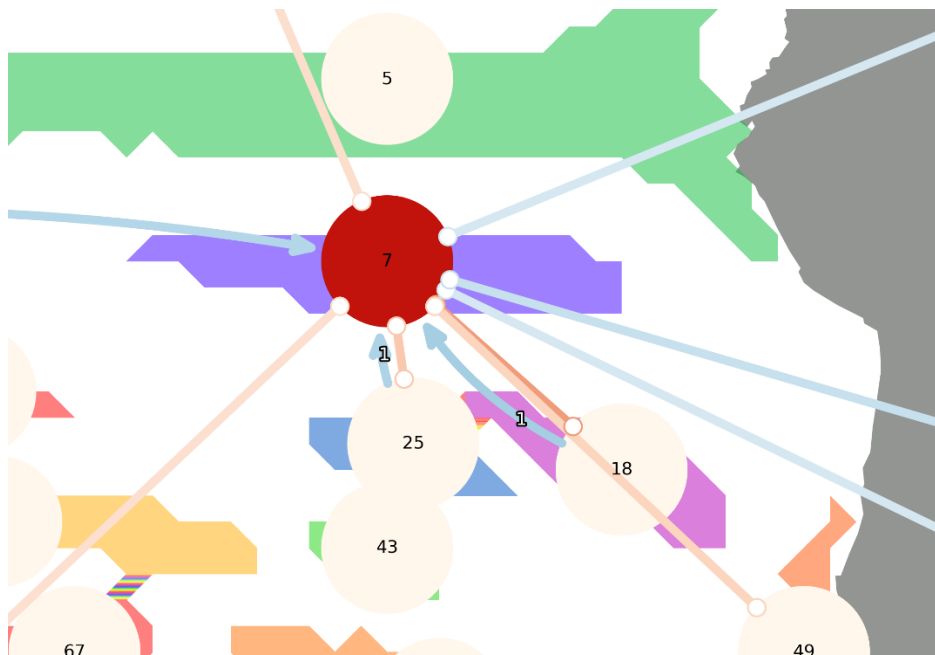


Figure 14: Contemporaneous (straight lines) and lagged edges (curved arrows) to and from Domain 7. Colours of the nodes and edges are the same as in Figure 5.

The Niño3.4 Index and SLA in Domain 7 are strongly correlated at a large range of lags ([figures in Supplementary](#)). ENSO appears to lead the SLA in Domain 7 (peak synchrony when ENSO leads by 4 months,  $R > 0.7$ ). Considering the proximity and an animation of SLA of the SEP (available in the [Supplementary](#)), diffusion processes appear to be a plausible explanation for an adjustment between the two domains on a timescale of several months. Another possible pathway for disturbances from ENSO to Domain 7 is through equatorial Kelvin waves, coastally trapped waves and finally ETRW.

Observations show that North of 15°S, ETRW propagate as far as 130°W (Li and Clarke. 2007), which corresponds to the longitude of the western edge of Domain 7, and travel  $\sim 6$  months from the coast to the centre of the Domain (observed phase speed of 24.4 cm s<sup>-1</sup>; Ramos et al. 2008).

Additionally, ENSO-related upwelling along the coast causes baroclinic instabilities of the coastal currents, promoting the generation of eddies (Holte et al. 2013; Conejero et al. 2020). Their mean direction is to the WNW/W (282 °/269 °) for anticyclonic/cyclonic eddies (Chaigneau and Pizarro. 2005) and may thus contribute to transfer disturbances from coastal waters offshore, especially during Eastern Pacific (EP) El Niño events. Conejero et al. (2020) have recently shown that during such events, the Eddy Kinetic Energy (EKE) is enhanced along the Peruvian coast, whereas Central Pacific El Niño and La Niña had little effect on the eddy generation, because of different Equatorial Kelvin Waves characteristics. However, eddies propagate about four times slower than ETRW at comparable latitudes (6 m s<sup>-1</sup> at 15°S) and only few rotate for several months (Chaigneau and Pizarro. 2005). Thus, some eddies generated along the coast may reach domain 7, their contribution to SLA in Domain 7 will likely be small.

Domain 7 lies within the Southeast Pacific Dry Zone and is a region a steady south-easterly trade winds with relatively small variability (Takahashi and Battisti. 2007; Chen and Wu. 2015). It is therefore likely that changes in the prevailing wind regime will cause SLAs. Indeed, SL in Domain 7 is significantly correlated to north-westerly to westerly winds stress in the west and south of the domain and within the domain itself, while no significant correlation was found between the domain signal and winds in the east and north of the domain (figures in [Supplementary](#)). This suggests that SLA are modulated by anomalies in local trade wind stress as well as strength and location of the SPSA, which normally produces south-easterly to easterly winds between Domains 7 and 25. During periods of decreased SPSA intensity and weaker-than-average easterly winds south of Domain 7, less southward Ekman transport can be expected, resulting in negative SLAs in Domain 25 and positive SLAs in Domain 25. This is supported by significant positive/negative correlations between SLP anomalies in Domain 18 (indicator for SPSA strength, see above) and SLA in Domains 25 and 7, respectively (Figure 12 and Figure 15). This may explain the negative cross-MCI between the two Domains in the PCMCI network at 1 month lead of Domain 25 (Figure 14). The large negative correlations at relatively high negative lags in Figure 15 may be attributed to indirect effects, since ENSO influences the strength of SPSA and SL at Domain 7 through different pathways and at different time lags.

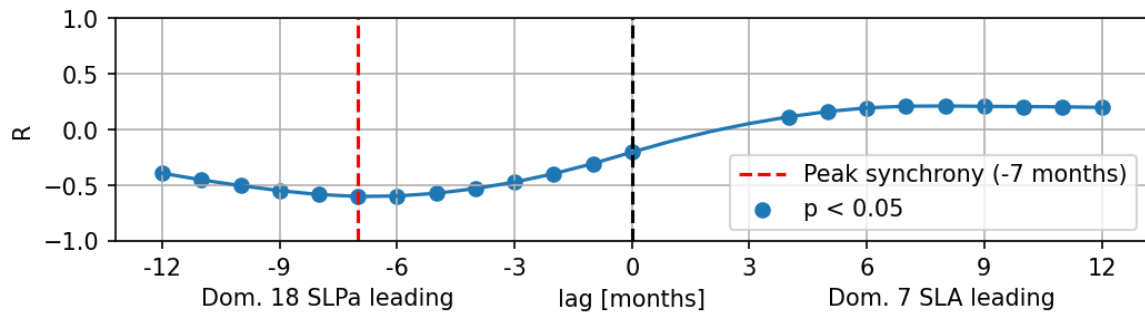


Figure 15: Lagged correlation between sea level pressure anomalies (SLPa) in Domain 18 (approx. position of the centre of the SPSA) and SLA in Domain 7. Meaning of points and lines is the same as in Figure 7.

No physical process that explains the significant positive zero-lag edge between domains 25 and 7 was found. This link may possibly occur because of temporarily shifted relationships during changed circulation patterns in the SEP related to the flavour of an ENSO event, similar to the shift observed between Domains 49 and 25. Due to the limited length of the internship, it was unfortunately not possible to investigate the drivers of this relationship in more detail.

Table 2 summarises the main contributors to SLV in the different domains identified in this study. This analysis clearly demonstrates the importance of ENSO in the Southeast Pacific by modulating both oceanic and atmospheric conditions, which subsequently trigger air-sea interactions. Globally, the network inferred by PCMCI is dominated by small lags (most edges have a lag of only one month, Figure 4), which suggests that most edges are results of atmospheric teleconnections. Oceanic connections (e.g. ETRW or eddies) are often much slower, as it has been discussed above.

*Table 2: Summary of the main influences in the different domains.*

Domain ID	Region	Influence
5	ETP	ENSO (mainly through wind stress)
49	Chilean coast	Coastal trapped Calvin waves (tropic origin) & local atmospheric forcing → Longshore winds influenced by SPSA (in turn modulated by ENSO)
25	W SPSA	Mainly SPSA and associated surface winds and advection. Flavour of ENSO may trigger specific atmospheric patterns.
7	SEP dry zone	Equatorial origin: diffusion and ETRWs (at lags of several months) Influence of SPSA intensity and associated surface winds and advection.

## 4 Limitations and Possible Ways Forward

The main limitation of this analysis was time since this project part of an internship of only 11 weeks. An in-depth investigation of the connections between SLAs in Domains 25 and 7 has to be done in the future.

Some limitations emerge from the AVISO sea level anomaly dataset used in this study. This product contains merged data from 13 satellites averaged over a month (AVISO. 2016), which increases the accuracy of the data. This temporal resolution makes it, however, hard to accurately track fast processes like atmospheric teleconnections or coastally trapped waves. Other datasets with considerably smaller timesteps (e.g. 5 days from NASA (Zlotnicki et al. 2019) or daily from Copernicus (Mertz and Legeais. 2020)) may potentially allow to resolve such processes better and infer directions of edges which appear contemporaneous in the AVISO dataset. The benefit of a better temporal resolution may, however, be offset by larger measurement errors and uncertainties resulting from the smaller amount of data and less sensor diversity per timestep.

Most lag times in the PCMCI network are very low, most of them are at only one month (Figure 4). This implies that fast processes like atmospheric teleconnections and air-sea interactions have a crucial role in the transport of disturbances. The SLA signal of Domains 7 is highly correlated and likely (almost) directly influenced by Domain 5 through relatively slow ETRW and diffusion at a lag of several months (see above). This link has not been discovered by PCMCI. Instead, it links the two Domains only indirectly connected through Domains 49 and 25. It is recalled that our dataset violated against the causal sufficiency assumption of PCMCI, since not all drivers are included in the dataset (e.g. atmospheric variables and SLA in parts of the ocean). Because of the causal sufficiency assumption, PCMCI orders the SEP Domains according to the temporal propagation of the disturbances. By this it appears to overlook the slower oceanic connection between Domains 5 and 7. In this context, it should also be highlighted, that large parts of the oceans are not covered by a Domain. An increased coverage by smaller domains that also cover parts between Domains 5 and 7 may have helped to identify this edge correctly but would at the same time increase the dimensionality of the dataset.

Furthermore, PCMCI does not account for the case that the relation between domains may change over time, like, for instance, between Domains 49 and 25 in response to the flavour of ENSO. It must be noted that the ENSO Domain (Domain 5) covers both the EP and CP region and no additional information on the flavour of ENSO was available in the dataset, which may have hindered the identification of this relation.

The network has been interpreted mainly with correlation analysis between SLA signals, flow, SLP and wind stress. Variations in SL were often explained by advection modulated by shallow-wind driven processes, which has already been identified to be among the main drivers in steric sea level variability by Piecuch and Ponte (2011). The authors note, however, that transport alone does often not close the SLV budget, and many processes may be at work simultaneously that amplifying or cancel out each other. Adding additional variables to the analysis (e.g., temperature, salinity) may to some extent help to overcome this constraint and allow to explore which other processes contribute to SL variations. A quantification of the importance of the different contributors directly from observational data will, however, likely be hard. For this task, a model-based estimations of the sea level budgets for each domain may be more suitable.

This study clearly shows the potential for causal discovery algorithms in complex systems. They can be a useful tool to enhance the understanding of the system, as long as the limitations that emerge from the method and the dataset are known. Even if causal discovery will not instantly solve the entire puzzle, it will help to solve parts of it and to formulate new questions.

## 5 Summary

In this study, more than 26 years of satellite altimetry measurements of sea level anomaly were analysed to investigate sea level variability in the Southeast Pacific. In a first step, all adjacent grid cells with a highly correlated temporal activity with the deltaMaps algorithm, which identified 101 SLV domains. Next, the PCMCI causal inference method was used to derive the global causal network between the different domains. A subset of this network from the Southeast Pacific has been analysed in more detail.

This subset consists of four nodes. This first corresponds to the ENSO region (Domain 5), while the others are located off the Chilean coast south of  $\sim 30^\circ\text{S}$  (Domain 49), a few degrees northwest of the average position of the Southeast Pacific Subtropical Anticyclone (SPSA) (Domain 25) and south of the ENSO region in the South Pacific Dry Zone (Domain 7).

The magnitude of SLV is greatest in Domain 5 and is primarily forced by wind anomalies associated with ENSO and its feedback cycles. A significant positive edge between Domains 5 and 49 exists at a lag of 1 and 2 months and can be explained mainly by an oceanic teleconnection in the form of coastal trapped waves which are regularly observed along the South American coast. Additionally, the strength of the SPSA, the dominant weather system in the Southeast Pacific, and the related wind patterns are negatively associated with ENSO. Resulting wind stress and Ekman transport anomalies amplify the remote equatorial forcing through the oceanic teleconnection off the Chilean coast.

PCMCI inferred a significantly positive edge between Domains 49 and 25 at lags of zero and one months, even though data analysis has shown that the relation between both domains shifts phase in response to the flavour of ENSO. SLV in Domain 25 appears to be primarily determined by advection in response to SPSA strength and position and related wind-driven processes. Especially during eastern Pacific ENSO events both SLA signals are anticorrelated. In contrast, central Pacific El Niño events trigger negative pressure and anti-clockwise wind stress anomalies around a centre at  $40\text{--}60^\circ\text{S}$  and  $100\text{--}120^\circ\text{W}$  that cause SLV in both Domain 49 and 25 to behave similarly. Many questions regarding

the atmospheric anomalies and related sea level responses remain and should be addressed in the future.

Domains 25 and 7 are connected through a positive edge at zero lag and a negative edge at one month lag. The negative edge can again be attributed to wind-stress anomalies associated with the SPSA. In in-depth investigation of the positive edge is still to be done. Surprisingly, PCMCi did not detect a link between Domains 5 (SLA in the ENSO region) and 7, which are likely connected through diffusion processes and Extratropical Rossby waves. This edge may have not been detected because of the slow nature of these processes and because the causal sufficiency assumption of PCMCi was not fulfilled by the dataset used.

Nevertheless, this study highlights the importance of the ENSO cycle in modulating SLV in the Southeast Pacific and the role of both oceanic and atmospheric teleconnections and air-sea interactions to transfer perturbations through an ocean basin. It was shown that the SLV network is not static and changes in response to the flavour of ENSO. This is not surprising, but has, to my best knowledge, not been discussed in the literature before and deserves more attention in the future.

The approach of this study, based on observational data and statistical analysis, enabled to infer the causal network of SLV. This does, however, not reveal the underlying processes that form this network. Methodological issues and the interpretation of the network only with wind, pressure and current data adds uncertainties and did not allow to quantify the different contributors of SLV. A joint approach using observational data to infer the network and regional modelling of SLV contributors may help to overcome this constraint and add further confidence in the results presented in this report.

## 6 Supplementary & Code

Python code to reproduce data, results and figures plots are available at [https://github.com/eikeschuett/dMaps\\_SLV](https://github.com/eikeschuett/dMaps_SLV). The supplementary figures and an animation of the AVISO SLA dataset for the study are also provided in the repository at [https://github.com/eikeschuett/dMaps\\_SLV/tree/main/figures/supplementary](https://github.com/eikeschuett/dMaps_SLV/tree/main/figures/supplementary).

## 7 References

- Ancapichun S, Garcés-Vargas J. 2015. Variability of the Southeast Pacific Subtropical Anticyclone and its impact on sea surface temperature off north-central Chile. *Ciencias Marinas* **41**(1): 1–20.
- AVISO. 2016. *SSALTO/DUACS User Handbook: MSLA and (M)ADT Near-Real Time and Delayed Time Products Issue 5.0*.
- Chaigneau A, Pizarro O. 2005. Eddy characteristics in the eastern South Pacific. *Journal of Geophysical Research* **110**(C6): 11,451.
- Chen Z, Wu L. 2015. Seasonal Variation of the Pacific South Equatorial Current Bifurcation. *Journal of Physical Oceanography* **45**(6): 1757–1770.
- Church JA, Aarup T, Woodworth PL, Wilson WS, Nicholls RJ, Rayner R, Lambeck K, Mitchum GT, Steffen K, Cazenave A, Blewitt G, Mitrovica JX, Lowe JA. 2010. Sea - Level Rise and Variability: Synthesis and Outlook for the Future. In *Understanding Sea-Level Rise and Variability*, Church JA, Woodworth PL, Aarup T, Wilson WS (eds). Wiley-Blackwell: Oxford, UK; 402–419.
- Conejero C, Dewitte B, Garçon V, Sudre J, Montes I. 2020. ENSO diversity driving low-frequency change in mesoscale activity off Peru and Chile. *Scientific reports* **10**(1): 17902.
- Dewitte B, Vazquez-Cuervo J, Goubanova K, Illig S, Takahashi K, Cambon G, Purca S, Correa D, Gutierrez D, Sifeddine A, Ortlieb L. 2012. Change in El Niño flavours over 1958–2008: Implications for the long-term trend of the upwelling off Peru. *Deep Sea Research Part II: Topical Studies in Oceanography* **77-80**(8): 143–156.



- Fahad AA, Burls NJ, Swenson ET, Straus DM. 2021. The Influence of South Pacific Convergence Zone Heating on the South Pacific Subtropical Anticyclone. *Journal of Climate* **34**(10): 3787–3798.
- Falasca F, Bracco A, Nenes A, Fountalis I. 2019. Dimensionality Reduction and Network Inference for Climate Data Using  $\delta$ -MAPS: Application to the CESM Large Ensemble Sea Surface Temperature. *Journal of Advances in Modeling Earth Systems* **11**(6): 1479–1515.
- Forget G, Ponte RM. 2015. The partition of regional sea level variability. *Progress in Oceanography* **137**(2): 173–195.
- Fountalis I, Dovrolis C, Bracco A, Dilkina B, Keilholz S. 2018.  $\delta$ -MAPS: From spatio-temporal data to a weighted and lagged network between functional domains. *Applied network science* **3**(1): 21.
- Fuenzalida R, Schneider W, Garcés-Vargas J, Bravo L. 2008. Satellite altimetry data reveal jet-like dynamics of the Humboldt Current. *Journal of Geophysical Research* **113**(C7): 1815.
- Granger CWJ. 1969. Investigating Causal Relations by Econometric Models and Cross-spectral Methods. *Econometrica* **37**(3): 424–438.
- Hamlington BD, Leben RR, Kim K-Y, Nerem RS, Atkinson LP, Thompson PR. 2015. The effect of the El Niño-Southern Oscillation on U.S. regional and coastal sea level. *Journal of Geophysical Research: Oceans* **120**(6): 3970–3986.
- Han W, Meehl GA, Stammer D, Hu A, Hamlington B, Kenigson J, Palanisamy H, Thompson P. 2017. Spatial Patterns of Sea Level Variability Associated with Natural Internal Climate Modes. *Surveys in geophysics* **38**(1): 217–250.
- Han W, Stammer D, Thompson P, Ezer T, Palanisamy H, Zhang X, Domingues CM, Zhang L, Yuan D. 2019. Impacts of Basin-Scale Climate Modes on Coastal Sea Level: A Review. *Surveys in geophysics* **40**(6): 1493–1541.
- Hersbach H, Bell B, Berrisford P, Hirahara S, Horányi A, Muñoz-Sabater J, Nicolas J, Peubey C, Radu R, Schepers D, Simmons A, Soci C, Abdalla S, Abellan X, Balsamo G, Bechtold P, Biavati G, Bidlot J, Bonavita M, Chiara G, Dahlgren P, Dee D, Diamantakis M, Dragani R, Flemming J, Forbes R, Fuentes M, Geer A, Haimberger L, Healy S, Hogan RJ, Hólm E, Janisková M, Keeley S, Laloyaux P, Lopez P, Lupu C, Radnoti G, Rosnay P, Rozum I, Vamborg F, Villaume S, Thépaut J-N. 2020. The ERA5 global reanalysis. *Quarterly Journal of the Royal Meteorological Society* **146**(730): 1999–2049.
- Holte J, Straneo F, Moffat C, Weller R, Farrar JT. 2013. Structure and surface properties of eddies in the southeast Pacific Ocean. *Journal of Geophysical Research: Oceans* **118**(5): 2295–2309.
- Hughes CW, Fukumori I, Griffies SM, Huthnance JM, Minobe S, Spence P, Thompson KR, Wise A. 2019. Sea Level and the Role of Coastal Trapped Waves in Mediating the Influence of the Open Ocean on the Coast. *Surveys in Geophysics* **40**(6): 1467–1492.
- Kao H-Y, Yu J-Y. 2009. Contrasting Eastern-Pacific and Central-Pacific Types of ENSO. *Journal of Climate* **22**(3): 615–632.
- Li J, Clarke AJ. 2007. Interannual Sea Level Variations in the South Pacific from 5° to 28°S. *Journal of Physical Oceanography* **37**(12): 2882–2894.
- Mertz F, Legeais JF. 2020. *Product User Guide and Specification: Sea Level v1.2*. [https://datastore.copernicus-climate.eu/documents/satellite-sea-level/D3.SL.1-v1.2\\_PUGS\\_of\\_v1DT2018\\_SeaLevel\\_products\\_v2.4.pdf](https://datastore.copernicus-climate.eu/documents/satellite-sea-level/D3.SL.1-v1.2_PUGS_of_v1DT2018_SeaLevel_products_v2.4.pdf). Accessed 11 June 2021.
- Meyssignac B, Piecuch CG, Merchant CJ, Racault M-F, Palanisamy H, MacIntosh C, Sathyendranath S, Brewin R. 2017. Causes of the Regional Variability in Observed Sea Level, Sea Surface Temperature and Ocean Colour Over the Period 1993–2011. *Surveys in Geophysics* **38**(1): 187–215.
- Moon J-H, Song YT, Lee H. 2015. PDO and ENSO modulations intensified decadal sea level variability in the tropical Pacific. *Journal of Geophysical Research: Oceans* **120**(12): 8229–8237.
- Nicholls RJ, Cazenave A. 2010. Sea-level rise and its impact on coastal zones. *Science (New York, N.Y.)* **328**(5985): 1517–1520.



- Oppenheimer M, Glavovic BC, Hinkel J, van de Wal RSW, Magnan AK, Abd-Elgawad A, Cai R, Cifuentes-Jara M, DeConto RM, Ghosh T, Hay J, Isla F, Marzeion B, Meyssignac B, Sebesvari Z. 2019. Chapter 4: Sea Level Rise and Implications for Low-Lying Islands, Coasts and Communities. In *IPCC Special Report on the Ocean and Cryosphere in a Changing Climate*, Pörtner HO, Roberts DC, Masson-Delmotte V, Zhai P, Tignor M, Poloczanska E, Mintenbeck K, Alegría A, Nicolai M, Okem A, Petzold J, Rama B, Weyer NM (eds): Geneva.
- Palanisamy H, Cazenave A, Meyssignac B, Soudarin L, Wöppelmann G, Becker M. 2014. Regional sea level variability, total relative sea level rise and its impacts on islands and coastal zones of Indian Ocean over the last sixty years. *Global and Planetary Change* **116**(2): 54–67.
- Peng Q, Xie S-P, Wang D, Zheng X-T, Zhang H. 2019. Coupled ocean-atmosphere dynamics of the 2017 extreme coastal El Niño. *Nature communications* **10**(1): 298.
- Piecuch CG, Ponte RM. 2011. Mechanisms of interannual steric sea level variability. *Geophysical Research Letters* **38**(15): 1739.
- Pizarro O, Clarke AJ, van Gorder S. 2001. El Niño Sea Level and Currents along the South American Coast: Comparison of Observations with Theory. *Journal of Physical Oceanography* **31**(7): 1891–1903.
- Pizarro O, Shaffer G, Dewitte B, Ramos M. 2002. Dynamics of seasonal and interannual variability of the Peru-Chile Undercurrent. *Geophysical Research Letters* **29**(12).
- Ramos M, Dewitte B, Pizarro O, Garric G. 2008. Vertical propagation of extratropical Rossby waves during the 1997–1998 El Niño off the west coast of South America in a medium-resolution OGCM simulation. *Journal of Geophysical Research* **113**(C8): 931.
- Ren Q, Li Y, Zheng F, Wang F, Duan J, Li R. 2020. Asymmetry of Interannual Sea Level Variability in the Western Tropical Pacific: Responses to El Niño and La Niña. *Journal of Geophysical Research: Oceans* **125**(10): 184.
- Runge J, Bathiany S, Bollt E, Camps-Valls G, Coumou D, Deyle E, Glymour C, Kretschmer M, Mahecha MD, Muñoz-Marí J, van Nes EH, Peters J, Quax R, Reichstein M, Scheffer M, Schölkopf B, Spirtes P, Sugihara G, Sun J, Zhang K, Zscheischler J. 2019a. Inferring causation from time series in Earth system sciences. *Nature communications* **10**(1): 2553.
- Runge J, Nowack P, Kretschmer M, Flaxman S, Sejdinovic D. 2019b. Detecting and quantifying causal associations in large nonlinear time series datasets. *Science advances* **5**(11): eaau4996.
- Takahashi K, Battisti DS. 2007. Processes Controlling the Mean Tropical Pacific Precipitation Pattern. Part II: The SPCZ and the Southeast Pacific Dry Zone. *Journal of Climate* **20**(23): 5696–5706.
- Tigramite. 2020. *Tigramite 4.2 documentation*. <https://jakobrunge.github.io/tigramite/>. Accessed 27 April 2021.
- Vega A, du-Penhoat Y, Dewitte B, Pizarro O. 2003. Equatorial forcing of interannual Rossby waves in the eastern South Pacific. *Geophysical Research Letters* **30**(5): n/a-n/a.
- Wang C, Deser C, Yu J-Y, DiNezio P, Clement A. 2017. El Niño and Southern Oscillation (ENSO): A Review. In *Coral Reefs of the Eastern Tropical Pacific: Persistence and Loss in a Dynamic Environment*, Enochs IC, Glynn PW, Manzello DP (eds). Springer Netherlands; Imprint: Springer: Dordrecht; 85–106.
- Wang Y, Gozolchiani A, Ashkenazy Y, Havlin S. 2016. Oceanic El-Niño wave dynamics and climate networks. *New Journal of Physics* **18**(3): 33021.
- Wiedermann M, Siegmund JF, Donges JF, Donner RV. 2021. Differential Imprints of Distinct ENSO Flavors in Global Patterns of Very Low and High Seasonal Precipitation. *Frontiers in Climate* **3**: 1481.
- Wilson AB, Bromwich DH, Hines KM, Wang S-h. 2014. El Niño Flavors and Their Simulated Impacts on Atmospheric Circulation in the High Southern Latitudes\*. *Journal of Climate* **27**(23): 8934–8955.
- You Y, Furtado JC. 2017. The role of South Pacific atmospheric variability in the development of different types of ENSO. *Geophysical Research Letters* **44**(14): 7438–7446.

- Yuan D, Hu X, Xu P, Zhao X, Masumoto Y, Han W. 2018. The IOD-ENSO precursory teleconnection over the tropical Indo-Pacific Ocean: Dynamics and long-term trends under global warming. *Journal of Oceanology and Limnology* **36**(1): 4–19.
- Zhang L, Han W, Li Y, Lovenduski NS. 2019. *Variability of Sea Level and Upper-Ocean Heat Content in the Indian Ocean: Effects of Subtropical Indian Ocean Dipole and ENSO*.
- Zlotnicki V, Qu Z, Willis J. 2019. *MEaSUREs Gridded Sea Surface Height Anomalies Version 1812*. [https://podaac.jpl.nasa.gov/dataset/SEA\\_SURFACE\\_HEIGHT\\_ALT\\_GRIDS\\_L4\\_2SATS\\_5DAY\\_6THDEG\\_V\\_JPL1812](https://podaac.jpl.nasa.gov/dataset/SEA_SURFACE_HEIGHT_ALT_GRIDS_L4_2SATS_5DAY_6THDEG_V_JPL1812).